

# Accretion of low angular momentum material onto black holes: 2D magnetohydrodynamical case.

Daniel Proga and Mitchell C. Begelman<sup>1</sup>

JILA, University of Colorado, Boulder, CO 80309-0440, USA; proga@colorado.edu, mitch@jila.colorado.edu

<sup>1</sup> also Department of Astrophysical and Planetary Sciences, University of Colorado at Boulder

## ABSTRACT

We report on the second phase of our study of slightly rotating accretion flows onto black holes. We consider magnetohydrodynamical (MHD) accretion flows with a spherically symmetric density distribution at the outer boundary, but with spherical symmetry broken by the introduction of a small, latitude-dependent angular momentum and a weak radial magnetic field. We study accretion flows by means of numerical 2D, axisymmetric, MHD simulations with and without resistive heating. Our main result is that the properties of the accretion flow depend mostly on an equatorial accretion torus which is made of the material that has too much angular momentum to be accreted directly. The torus accretes, however, because of the transport of angular momentum due to the magnetorotational instability (MRI). Initially, accretion is dominated by the polar funnel, as in the hydrodynamic inviscid case, where material has zero or very low angular momentum. At the later phase of the evolution, the torus thickens towards the poles and develops a corona or an outflow or both. Consequently, the mass accretion through the funnel is stopped. The accretion of rotating gas through the torus is significantly reduced compared to the accretion of non-rotating gas (i.e., the Bondi rate). It is also much smaller than the accretion rate in the inviscid, weakly rotating case. Our results do not change if we switch on or off resistive heating. Overall our simulations are very similar to those presented by Stone, Pringle, Hawley and Balbus despite different initial and outer boundary conditions. Thus, we confirm that MRI is very robust and controls the nature of radiatively inefficient accretion flows.

*Subject headings:* accretion – magnetohydrodynamics – black hole physics – outflows – galaxies: active – methods: numerical

## 1. Introduction

Accretion onto supermassive black holes (SMBHs) very likely powers some of the most dramatic phenomena of astrophysics, such as quasars and powerful radio galaxies. However, SMBH accretion does not always result in high radiative output, as evidenced by SMBHs that appear to spend most of their time in a remarkably quiescent state (e.g., Di Matteo et al. 1999, 2000, 2001; Loewenstein et al. 2001; for Sgr A\*, see review by Melia & Falcke 2001). Dim SMBHs are not something one would expect, because

these black holes are embedded in the relatively dense environments of galactic nuclei. Therefore it is natural to suppose that the gravity due to an SMBH will draw in matter at high rates, leading to a high system luminosity.

Estimates for the accretion luminosity,  $L$ , rely on assumptions about the mass accretion rate,  $\dot{M}_a$ , and the efficiency of transforming the gas energy into radiation,  $\eta$  (i.e.,  $L = \eta c^2 \dot{M}_a$ ). Both  $\dot{M}_a$  and  $\eta$  are uncertain and there is no generally accepted model which could explain low luminosity SMBHs by predicting low enough  $\dot{M}_a$  or  $\eta$ , or both.

The result that SMBHs are dimmer than they should be is primarily due to the fact that we estimate  $\dot{M}_a$  based on the density and temperature of the gas in which the SMBHs are embedded. It is customary to adopt the analytic formula due to Bondi (1952) to estimate the mass accretion rate. Bondi (1952) considered spherically symmetric accretion from a non-rotating polytropic gas with uniform density  $\rho_\infty$  and sound speed  $c_\infty$  at infinity. Under these assumptions, a steady state solution to the equations of mass and momentum conservation exists with a mass accretion rate of

$$\dot{M}_B = \lambda 4\pi R_B^2 \rho_\infty c_\infty, \quad (1)$$

where  $\lambda$  is a dimensionless parameter that, for the Newtonian potential, depends only on the adiabatic index. The Bondi radius,  $R_B$ , is defined as

$$R_B = \frac{GM}{c_\infty^2}, \quad (2)$$

where  $G$  is the gravitational constant and  $M$  is the mass of the accretor.

Relatively high  $\dot{M}_a$  predicted by the Bondi formula is partially responsible for generating a lot of interest in accretion flows with low  $\eta$ , that is, where transfer of the flow internal energy to radiation is very inefficient. Nonradiative accretion flow solutions are possible because binding energy dissipated in the gas can be advected through the event horizon before being radiated (Ichimaru 1977; Rees et al. 1982; Narayan & Yi 1994, 1995; Abramowicz et al. 1995).

Neglect of radiative cooling in accretion flows does not lead to just one family of solutions, however. In particular, the above-mentioned pure advection-dominated inflows constitute only one possible class of solutions. Once rotation is allowed, radiatively inefficient hydrodynamical (HD) flows become subject to strong convection (Begelman & Meier 1982; Narayan & Yi 1995), which can fundamentally change the flow pattern and its radiative properties (Igumenshchev & Abramowicz 1999; Blandford & Begelman 1999; Stone, Pringle & Begelman 1999; Quataert & Narayan 1999; Narayan, Igumenshchev & Abramowicz 2000; Quataert & Gruzinov 2000). Numerical and theoretical studies show that convection alters the steep ( $\propto r^{-3/2}$ ) density profile of advection-dominated flows into a much flatter ( $\propto r^{-1/2}$ ) profile, which can explain the faintness of many SMBHs because it predicts relatively low density close to the black hole (i.e.,  $\dot{M}_a$  is low in eq. 1). Similar structural changes occur in the magnetohydrodynamical (MHD) limit (Stone & Pringle 2001, SP01 hereafter; Hawley, Balbus, & Stone 2001; Machida, Matsumoto & Mineshige 2001; Igumenshchev & Narayan 2002; Hawley & Balbus 2002), although here the turbulence is probably driven by magnetorotational instability (MRI) rather than thermal convection (Balbus & Hawley 2002; but see Abramowicz et al. 2002 and Narayan et al. 2002 for alternative views).

The turbulent character of both HD and MHD models does not settle the issue of what happens to the energy and angular momentum that must be transported away. There are two possibilities: (i) turbulent transport effectively shuts off the accretion flow, turning it into a closed circulation (Narayan et al. 2000; Quataert & Gruzinov 2000) or (ii) turbulent transport drives powerful outflows that can strongly modify

the black hole’s environment (Narayan & Yi 1994, 1995; Blandford & Begelman 1999). Recent MHD simulations bring new insights that may help us to resolve this issue. For example, Hawley & Balbus’s (2002) three-dimensional MHD simulations show that, with and without resistive heating, some mass and energy in nonradiative accretion flows are carried off by an outflow in keeping with the outline of the second possibility.

An important element of the problem of very low SMBH luminosity is the rate at which mass is captured into the accretion flow. If this rate is far lower than  $\dot{M}_B$ , then the problem of very low SMBH luminosity becomes less severe. SMBHs draw matter from an extended medium and most authors assume that the Bondi (1952) formula provides an adequate approximation for the rate of mass supply. Evolution of the flow already captured by an SMBH has been studied extensively, but evolution of the flow including regions beyond the domination of gravity has not been given its due. The Bondi formula has been derived under the assumption that this gas is non-rotating and only under the influence of the central gravity. Thus, for a given gravitational field, the gas internal energy determines the accretion rate. By relaxing this assumption, introducing additional forces or sources of energy, one may find that the mass supply rate is much lower than the one predicted by the Bondi formula. For example, the rate at which matter is captured by a black hole can be severely limited when the matter is heated by X-rays produced near the black hole (Ostriker et al. 1976) or by mass outflow from the central region (Di Matteo et al. 2003; Fabbiano et al. 2003). In these two cases, the gas internal energy is increased. Introducing kinetic energy to the gas at infinity may have a similar effect: although the flow outside the Bondi accretion radius often can be described as nonrotating, even a tiny amount of angular momentum,  $l$  — when followed inward — could severely limit the rate at which matter is captured by the black hole (e.g., Proga & Begelman 2003, PB03 hereafter, and references therein).

In PB03, we reported on the first phase of our study of slightly rotating accretion flows onto black holes. We considered inviscid, hydrodynamic accretion flows with a spherically symmetric density distribution at the outer boundary, but with spherical symmetry broken by the introduction of a small, latitude-dependent angular momentum. Namely we assumed that at the outer radial boundary, the specific angular momentum,  $l$ , depends on the polar angle,  $\theta$ , as

$$l(\theta) = l_0 f(\theta), \quad (3)$$

where  $f = 1$  on the equator ( $\theta = 90^\circ$ ) and monotonically decreases to zero at the poles ( $\theta = 0^\circ$  and  $180^\circ$ ). PB03’s main result was that the properties of the accretion flow do not depend as much on the outer boundary conditions (i.e., the amount as well as distribution of the angular momentum parameterized by  $l_0$  and the form of  $f$ ) as on the geometry of the non-accreting matter. The material that has too much specific angular momentum to be accreted ( $l > 2R_S c$ , where  $R_S = 2GM/c^2$  is the radius of a Schwarzschild black hole) forms a thick torus near the equator. Consequently, the geometry of the polar region, where material is accreted (the funnel), and the mass accretion rate through it are constrained by the size and shape of the torus. PB03’s results showed one way in which the mass accretion rate of slightly rotating gas can be significantly reduced compared to the accretion of non-rotating gas (i.e., the Bondi rate), and set the stage for calculations that will take into account the transport of angular momentum and energy as presented here.

We report on the second phase of our study and assess the gross properties of rotating accretion flows onto black holes with the inclusion of MHD effects. We consider a classic Bondi accretion flow modified by the introduction of (i) a small, latitude-dependent angular momentum at infinity, (ii) a pseudo-Newtonian gravitational potential and (iii) weak magnetic field. The imposed angular momentum and magnetic field are weak enough to have initially a negligible effect on the density distribution at the outer boundary, which

remains spherically symmetric. Contrary to PB03, we now consider the transport of energy and angular momentum by including magnetic field effects. Therefore our model allows for accretion of matter which initially has a specific angular momentum higher than  $2R_{Sc}$ . Yet we still consider a simple model of an accretion flow, simpler than those occurring in nature, as we neglect the gravitational field due to the host galaxy, radiative heating and cooling effects and 3D effects of MHD.

Our work is complementary to some other previous studies. Several authors considered accretion onto black holes with a focus on the evolution of rotationally supported thick tori including the transport of angular momentum and energy (e.g., Igumenshchev & Abramowicz 1999; SP01; Machida et al. 2001; Hawley & Balbus 2002; McKinney & Gammie 2002; Igumenshchev, Narayan & Abramowicz 2003). The main difference between our work and these studies is that our simulations have one degree of freedom more than the previous studies. The other authors consider cases where if not for the transport of angular momentum due to internal stresses, there would be neither time evolution nor mass accretion. For example, for their initial conditions Stone et al. (1999), SP01, Hawley & Balbus (2002), and Igumenshchev et al. (2003) adopted a bounded torus in hydrostatic equilibrium with uniform angular momentum, embedded in zero angular momentum ambient gas which is also in hydrostatic equilibrium. The zero- $l$  ambient gas has a very low density and is unimportant dynamically. Thus previous studies consider accretion from a finite reservoir of gas that is not refilled during simulations. On the other hand, we allow time evolution and mass accretion, even without internal stresses. We start our simulations from a radial inflow and allow for gas with a constant density but a range of angular momenta to enter the computational domain during simulations. Thus, our flow is a complex convolution of rotating and non-rotating flows with similar densities that may be sub-Keplerian over a very large range of radii. We find that despite these differences the accretion through the torus, facilitated by MRI, dominates the inner flow. Thus, our results reinforce the findings of the previous studies.

We note that if the low- $l$  material were allowed to accrete onto the black hole then it could significantly contribute to the total mass accretion rate. However, detailed simulations are required to check what will happen in such a situation. Here we report on quite intriguing results, especially when compared to the HD inviscid simulations: the low- $l$  material that can be accreted in the inviscid case (with no need for any transport of  $l$ ) is *not* accreted in the MHD case, whereas the high- $l$  material that could not be accreted in the inviscid case, is accreted in the MHD case. This seemingly paradoxical behavior can be understood by the fact that the energy and angular momentum from the MHD torus are deposited outside the torus in the polar region (see, e.g., Stone et al. 1999; Blandford & Begelman 1999; Blandford & Begelman 2002a, 2002b; Hawley & Balbus 2002), effectively choking off the funnel. In PB03, we speculated that this energy and angular momentum might interfere with the inflow in the funnel. But it was unclear whether this would lead to a significant net reduction of  $\dot{M}_a$ , especially when the compensating inflow in the torus was taken into account. The simulations we present here suggest that the compensation is negligible, and that the total accretion rate is far lower than in the inviscid case with a similar angular momentum distribution at infinity.

The outline of this paper is as follows. We describe our calculations in Section 2. In Section 3, we present our results. We summarize our results and discuss them together with their limitations in Section 4.

## 2. Method

### 2.1. Equations

To calculate the structure and evolution of an accreting flow, we solve the equations of magnetohydrodynamics

$$\frac{D\rho}{Dt} + \rho\nabla \cdot \mathbf{v} = 0, \quad (4)$$

$$\rho \frac{D\mathbf{v}}{Dt} = -\nabla P - \rho\nabla\Phi + \frac{1}{4\pi}(\nabla \times \mathbf{B}) \times \mathbf{B}, \quad (5)$$

$$\rho \frac{D}{Dt} \left( \frac{e}{\rho} \right) = -P\nabla \cdot \mathbf{v} + \eta_r \mathbf{J}^2, \quad (6)$$

$$\frac{\partial \mathbf{B}}{\partial t} = \nabla \times (\mathbf{v} \times \mathbf{B} - \eta_r \mathbf{J}), \quad (7)$$

where  $\rho$  is the mass density,  $P$  is the gas pressure,  $\mathbf{v}$  is the fluid velocity,  $e$  is the internal energy density,  $\Phi$  is the gravitational potential,  $\mathbf{B}$  is the magnetic field vector,  $\mathbf{J}$  is the current density, and  $\eta_r$  is an anomalous resistivity. We adopt an adiabatic equation of state  $P = (\gamma - 1)e$ , and consider models with  $\gamma = 5/3$ . Our calculations are performed in spherical polar coordinates  $(r, \theta, \phi)$ . We assume axial symmetry about the rotational axis of the accretion flow ( $\theta = 0^\circ$  and  $180^\circ$ ).

We present simulations using the pseudo-Newtonian potential  $\Phi$  introduced by Paczyński & Wiita (1980)

$$\Phi = -\frac{GM}{r - R_S}. \quad (8)$$

This potential approximates general relativistic effects in the inner regions, for a nonrotating black hole. In particular, the Paczyński–Wiita (WP) potential reproduces the last stable circular orbit at  $r = 3R_S$  as well as the marginally bound orbit at  $r = 2R_S$ .

To compute resistivity, we follow SP01:

$$\eta_r = Q(\Delta x)^2 |\mathbf{J}| / \sqrt{\rho}, \quad (9)$$

where  $\Delta x$  is the grid spacing and  $Q$  is a dimensionless constant. We also follow SP01 in adopting  $Q = 0.1$ .

## 2.2. Initial conditions and boundary conditions

For the initial conditions of the fluid variables we follow PB03 and adopt a Bondi accretion flow with zero angular momentum everywhere except for the outermost part of the flow. In particular, we adopt  $v_\theta = 0$  while  $v_r$  and  $\rho$  are computed using the Bernoulli function and mass accretion rate for spherically symmetric Bondi accretion with the PW potential. We set  $\rho_\infty = 1$  and specify  $c_\infty$  through  $R'_S \equiv R_S/R_B$  (note that  $R'_S = 2c_\infty^2/c^2$ ). We specify the initial conditions by adopting a non-zero specific angular momentum  $l$  for the outer subsonic part of the flow.

We consider a general case where the angular momentum at the outer radius  $r_o$  depends on the polar angle via

$$l(r_o, \theta) = l_0 f(\theta), \quad (10)$$

with  $f = 1$  on the equator ( $\theta = 90^\circ$ ) and  $f = 0$  at the poles ( $\theta = 0^\circ$  and  $180^\circ$ ). We express the angular momentum on the equator as

$$l_0 = \sqrt{R'_C R_B} c_\infty, \quad (11)$$

where  $R'_C$  is the “circularization radius” on the equator in units of  $R_B$  for the Newtonian potential (i.e.,  $GM/r^2 = v_\phi^2/r$  at  $r = R'_C R_B$ ).

We adopt one form for the function  $f(\theta)$ :

$$f_3(\theta) = \begin{cases} 0 & \text{for } \theta < \theta_o \text{ and } \theta > 180^\circ - \theta_o \\ l_0 & \text{for } \theta_o \leq \theta \leq 180^\circ - \theta_o. \end{cases} \quad (12)$$

We call this function  $f_3$  to be consistent with the nomenclature in PB03.

We generate the initial magnetic field using a vector potential, i.e.,  $\mathbf{B} = \nabla \times \mathbf{A}$ . We consider one straightforward initial magnetic configuration: a purely radial field defined by the potential  $\mathbf{A} = (A_r = 0, A_\theta = 0, A_\phi = A \cos \theta / r \sin \theta)$ . We scale the magnitude of the magnetic field using a parameter,  $\beta_o \equiv 8\pi P_B(r_o)/B^2$  defined as the plasma parameter  $\beta \equiv 8\pi P/B^2$  at the outer boundary,  $r_o$ , so that

$$A = \text{sign}(\cos \theta) \sqrt{(8\pi P_B(r_o)/\beta_o) r_o^2}, \quad (13)$$

where  $P_B$  is the gas pressure associated with the Bondi solution at  $r_o$ . Note that the magnetic field changes sign across the equator.

Our standard computational domain is defined to occupy the radial range  $r_i = 1.5 R_S \leq r \leq r_o = 1.2 R_B$  and the angular range  $0^\circ \leq \theta \leq 180^\circ$ . We consider models with  $R'_S = 10^{-3}$ . The  $r - \theta$  domain is discretized into zones with 140 zones in the  $r$  direction and 100 zones in the  $\theta$  direction. We fix zone size ratios,  $dr_{k+1}/dr_k = 1.05$ , and  $d\theta_l/d\theta_{l+1} = 1.0$  for  $0^\circ \leq \theta \leq 180^\circ$ . However, we have also performed some runs with  $d\theta_l/d\theta_{l+1} = 1.02$  for  $0^\circ \leq \theta \leq 90^\circ$  and  $d\theta_{l+1}/d\theta_l = 1.02$  for  $90^\circ \leq \theta \leq 180^\circ$  (i.e., the zone spacing is decreasing toward the equator).

The boundary conditions are specified as follows. At the poles, (i.e.,  $\theta = 0^\circ$  and  $180^\circ$ ), we apply an axis-of-symmetry boundary condition. At both the inner and outer radial boundaries, we apply an outflow boundary condition for all dynamical variables except the magnetic field. For the magnetic field at the outer boundary, we apply an outflow condition, whereas at the inner boundary, we follow SP01 and use a negative stress condition (i.e., we enforce  $B_r B_\phi \leq 0$  at  $r = r_i$ ). We also ran some models using an outflow condition for the magnetic field at the inner boundary and found similar results. As in PB03, to represent steady conditions at the outer radial boundary, during the evolution of each model we continue to apply the constraints that in the last zone in the radial direction,  $v_\theta = 0$ ,  $v_\phi = l_0 f(\theta)/r \sin \theta$ , and the density is fixed at the Bondi value at all times. Note that we allow  $v_r$  to float. Additionally, we fix the magnetic field at its initial radial configuration in the last zone in the radial direction (i.e.,  $B_r = \frac{1}{r \sin \theta} \frac{\partial(A_\phi \sin \theta)}{\partial \theta}$ ,  $B_\theta = 0$  and  $B_\phi$  is allowed to float). To reduce the problems caused by very high Alfvénic velocities in regions of very low density (i.e., to prevent the time step from being prohibitively small), we set a lower limit to the density on the grid as  $\rho_{min}(r) = \sqrt{r_i/r}$  and enforce it at all times in all models.

To solve eqs. (4)-(7) we use the ZEUS-2D code described by Stone & Norman (1992a, 1992b), modified to implement the PW potential and resistive heating.

### 3. Results

We specify our model by several parameters. We set the length scale in terms of the black hole radius in units of the Bondi radius,  $R'_S$ . Our second parameter is the adiabatic index,  $\gamma$ . The third parameter (or

a function rather) is the angular momentum at the outer radial boundary,  $l = l_0 f(\theta)$ . The last parameter is the plasma parameter at the outer boundary,  $\beta_o$ .

For practical reasons, we consider a relatively large value of  $R'_S = 10^{-3}$  (see PB03 and below for reasons why  $R'_S < 10^{-3}$  is not suitable for our purposes). Our choice of  $R'_S$  allows us to run our models over a couple of dynamical time scales at large radii and therefore obtain solutions which have lost memory of the initial conditions. We consider flows with  $\gamma = 5/3$ . Note that we allow the entropy of gas to increase due to nonadiabatic heating caused by the artificial viscosity and the resistivity (The artificial viscosity is a compressible bulk viscosity, not a shear viscosity, and does not affect rotation of the flow [Stone & Norman 1992a]). We assume an angular momentum distribution at the outer radial boundary as described in Section 2. We focus our attention on accretion of matter with low angular momentum, i.e., where the corresponding centrifugal force is small compared to gravity for all  $\theta$  at the Bondi radius (see PB03 for details). Finally, we consider weak magnetic fields only. Our choice for the magnetic field strength is dictated by the requirement that the flow be initially super-Alfvénic in the entire computational domain:  $|v_p| > |v_{Ap}|$ , for all radii, where  $v_p \equiv \sqrt{v_r^2 + v_\theta^2}$  is the poloidal fluid velocity and  $v_{Ap} \equiv \sqrt{(B_r^2 + B_\theta^2)/4\pi\rho}$  is the poloidal Alfvén velocity.

Table 1 summarizes the properties of the simulations we discuss here. Columns (2) through (7) give the numerical resolution in the radial direction; the black hole radius compared to the Bondi radius,  $R'_S$ ; the circularization radius compared to the Bondi radius,  $R'_C$ ; the specific angular momentum on the equator at  $r = r_o$ ,  $l_0$ , in units of  $2R_{Sc}$ ; the width of the angular distribution for which  $l \leq 2R_{Sc}$ ,  $\theta_o$ ; and the angular momentum dependence on the polar angle at the outer boundary,  $f(\theta)$ , respectively. Columns (8) and (9) give the plasma parameter at the outer boundary,  $\beta_o$ , and the dimensionless constant of the anomalous resistivity,  $Q$ , respectively. Table 1 also presents the final time at which we stopped each simulation (all times here are in units of the Keplerian orbital time at  $r = R_B$ ), the range within which the maximum specific angular momentum at the inner radial boundary varies at the end of the simulation,  $l_a^{max}$ , and the mass accretion rate through the inner radial boundary measured near the end of the simulation, in units of the corresponding Bondi accretion rate. The mass accretion rate is time-averaged over 0.2 orbits at the end of each simulation, except for run C where it is averaged for 0.05 orbits only. Finally, column (13) gives comments about runs different from the standard runs (e.g., higher spatial resolution in the  $\theta$  direction near the equator).

Our simulations show that for  $l_0 \geq 2R_{Sc}$  the accretion flow consists of an equatorial torus with MHD turbulence driven by MRI. The latter produces accretion through the torus. The MHD turbulent torus also determines the fate of the material in the polar funnel, where  $l < 2R_{Sc}$  and could be accreted directly. For cases with a very weak magnetic field or more generally at the beginning of simulations, there is supersonic funnel accretion as in the inviscid HD case. However, as MRI in the torus grows, the torus thickens and an outflow from the torus develops. As a result, the torus or its wind closes the polar funnel and quenches the accretion through the funnel. We describe an example of such an accretion flow in some detail first (Section 3.1). This is followed by a limited parameter survey in which we focus on varying two key aspects of our models: the strength of the magnetic field and the angular distribution of angular momentum on the outer boundary.

### 3.1. Accretion flow consisting of an MHD torus

In this section we describe the properties and behavior of our model in which  $R'_S = 10^{-3}$ ,  $\beta_o = 10^6$ , and a step function describes the angular distribution of angular momentum on the outer boundary (run D). We assume that for  $45^\circ \leq \theta \leq 135^\circ$ , the specific angular momentum on the equator at the outer boundary equals  $2R_{Sc}$ , whereas for  $\theta < 45^\circ$  and  $\theta > 135^\circ$ ,  $l = 0$ . This angular distribution of  $l$  on the outer boundary uses the same  $\theta_o$  as the fiducial model in PB03 (i.e., model B04f1a) for which  $R'_C = 0.1$  and  $f(\theta) = 1 - |\cos \theta|$ . Thus we assume that the material that cannot be accreted onto the black hole, without angular momentum transport, is located (at the outer boundary) relatively close to the equator. Inversely, we consider a relatively wide polar funnel containing zero- $l$  material. Our run H is the HD inviscid counterpart of run D and serves as a reference run.

Figure 1 presents a sequence of density and angular velocity contours, and the direction of the fluid velocity for run D. After a transient episode of infall, the gas with  $l = 2R_{Sc}$  piles up outside the black hole and forms a thick torus bounded by a centrifugal barrier near the rotation axis. Soon after the torus forms (i.e., a couple of orbits at  $r = r_i$ ), the magnetic field is amplified both by MRI and by shear. The torus starts evolving rapidly and accretes onto the black hole. Another important effect of magnetic fields is that the torus produces a magnetized corona and an outflow. By a corona we mean gas outside a torus, with a low  $\beta$  ( $\lesssim 0.1$ ), density lower than in the torus by one or more orders of magnitude, and with vigorous circulation (see the top panels in Figure 8 for a good illustration of the torus and corona). On the other hand, by an outflow we mean gas with a systematic poloidal velocity directed away from the equator and the black hole. Initially, the role of the corona and outflow is negligible. For example, at the early phase of the evolution,  $0.1 \lesssim t \lesssim 0.4$ , the low- $l$  material close to the axis can accrete almost steadily through a funnel despite the torus corona and outflow (see Fig. 4). The mass accretion rate during this phase is dominated by the low- $l$  material and is similar to  $\dot{M}_a$  for a pure HD inviscid flow where accretion occurs only through the polar funnel. The accretion rate due to the torus is  $\gtrsim 1$  orders of magnitude lower than  $\dot{M}_a$  due to the polar funnel. But at the later phase,  $t > 0.5$ , the MHD turbulent corona of the torus expands toward the poles and the torus outflow becomes stronger. They both eventually shut off the polar funnel accretion. Note that the polar outflow (‘jet’) reaches the outer boundary by  $t \sim 0.5$ . A shock wave, associated with a transient, propagates outward through the entire computational domain during the first dynamical time scale. After the shock wave passes through the outer boundary, the flow in the torus is subsonic, highly variable and is directed inward near the equator and outward close to the poles. We note that the flow with non-zero angular momentum keeps rotating on cylinders over the whole simulation regardless of how complex is the velocity field. We shall return to this point below. Also we note that at the end of the simulation, the angular distribution of captured mass differs significantly from the spherically symmetric Bondi accretion flow. Only gas which enters the computational domain near the equator reaches the inner part of the domain. We will show the inner part of the flow and discuss its nature below. However, it is clear even from Fig. 1 that some of the equatorial inflow does not make it into the black hole but rather turns around and leaves the computational domain through the outer boundary.

To provide some insight into the time dependence, Figures 2 and 3 show the time evolution of the mass accretion rate in units of the corresponding Bondi rate. Initially,  $\dot{M}_a$  drops from 1 to 0.03 at  $t = 0.1$ . Then it rises sharply by one order of magnitude and starts oscillating irregularly between  $\sim 0.003$  and  $\sim 0.03 - 0.1 \dot{M}_a/\dot{M}_B$  for the remainder of the simulation. Figure 3a shows that toward the end of simulation,  $\dot{M}_a(t)$  has settled into a pattern that can be characterized as follows:  $\dot{M}_a$  sharply increases, then decreases gradually by  $\sim 1$  order of magnitude to an almost steady level and then increases sharply again. These sharp increases and gradual decreases are quasi-periodic and reoccur about every 0.07 orbits. Figure 3a shows also that on the top of this quite regular pattern of ‘bursts’ and exponential ‘declines’ there are short-lived ‘dips’ and ‘spikes’. In summary, the time-dependence and level of accretion via the torus



appear to have reached a persistent state.

To show the complex structure of the flow at small radii and gain some insight into the very highly time-dependent evolution of the mass accretion rate, Figures 4–7 and Figure 8 compare the inner accretion flow at four different times when a) accretion occurs through the torus and polar funnel ( $t = 0.22$ , Fig. 4 and the top left panel in Fig. 8); b) accretion occurs only through the torus ( $t = 2.39$ , Fig. 5 and the top right panel in Fig. 8); c) accretion through the torus is quenched by the strong magnetic field which forms a magnetized polar cylinder around the black hole; ( $t = 2.41$ , Fig. 6 and the bottom left panel of Fig. 8); and d) accretion of low- $l$  material occurs through the polar region outside the torus ( $t = 2.36$ , Fig. 7 and the bottom right panel of Fig. 8). Figures 4–7 plot snapshots of the density, entropy,  $S \equiv \ln(P/\rho^\gamma)$ , angular velocity, specific angular momentum, and direction of the fluid velocity (top panels from left to right) and the total pressure,  $P_{tot} = P + B^2/8\pi$ , magnetic pressure,  $P_{mag} = B^2/8\pi$ , plasma parameter,  $\beta$ , toroidal magnetic field, and direction of the magnetic field (bottom panels from left to right). To display the generic features of run D in its four states in a more compact form, Fig. 8 compares only snapshots of the density over-plotted by the direction of the fluid velocity. Note vertical arrows on Figure 2 and Figure 3a which mark the times for these four snapshots: arrows a, b, c, d correspond to Figs. 4, 5, 6 and 7 (and top left, top right, bottom left and bottom right panels in Fig. 8), respectively.

Figure 4 shows the inner flow characteristic of the early phase of the evolution ( $0.1 \lesssim t \lesssim 0.4$ ). The torus made of high- $l$  material accretes onto the black hole due to MRI. The torus produces a magnetized corona with vigorous circulation bounded by the low- $l$  material accreting onto the black hole through the polar funnel. The flow at this stage is similar to its HD inviscid counterpart because the polar funnel accretion is dominant and its  $\dot{M}_a$  is determined by the shape of the torus. There are two qualitative differences between run D in this early phase and its HD inviscid counterpart. In run D, the torus also accretes but at much lower rate than the funnel. In the HD inviscid case there is no torus accretion at all. The shape of the funnel in run D is also affected by the torus corona, albeit slightly. However, as the torus corona and outflow grow, the above mentioned differences become important.

Figure 5 shows the inner flow at a later phase of the evolution, when the corona and outflow have fully developed and can block the low- $l$  material incoming in the polar funnel. At this point accretion is due only to the torus and  $\dot{M}_a$  is at an intermediate level. During this intermediate  $\dot{M}_a$  state, matter is accreted via a torus extending down to the inner boundary. There can also be some accretion through the polar funnel but its rate is very low and the actual value of the accretion rate via the funnel is determined by the density floor we imposed (see Section 1). For small radii, the polar funnel is “empty” because the torus outflow extends to the poles at large radii and shuts off the mass supply. However, the polar funnel has a significant pressure due to the magnetic field. In fact, the total pressure distribution is close to spherical despite the huge change in the gas pressure as we go from the poles to the equator for a given radius. The torus is time-variable due to the MHD turbulence. In particular, the density of the accreted material fluctuates and once it becomes too low, the magnetic field in the polar funnel can expand toward the equator and reconnect. At that instant the torus is pushed outward by the magnetic field and  $\dot{M}_a$  drops until the gas in the torus piles up and squashes the magnetic field (compare Figure 5 and 6). Fig. 6 shows that at very small radii, the magnetic field is vertical in this state instead of being radial as during other states shown. Each ‘dip’ in the accretion rate is followed by a ‘spike’ during which the torus unloads the material piled up during the dip.

The strong time variability of the inner accretion flow affects also the outer accretion flow. For example, the torus corona and outflow struggle constantly with the low- $l$  material in the polar region. This material has neither rotational nor pressure support and therefore it would accrete if not for the torus corona and

outflow. However, the torus corona and outflow sometimes become too weak to prevent the low- $l$  material from accreting. When this happens we observe a burst of accretion. Figure 7 illustrates such a burst. Note a low- $l$  stream reaching the inner boundary below the equator. It takes a relatively long time ( $\sim 0.03$  orbits) for the torus corona and outflow to push this stream of low- $l$  material away. Therefore  $\dot{M}_a$  decreases gradually with time to the level determined by the accretion rate due to the torus alone.

We conclude that the time-dependent accretion in run D is due to unsteady accretion via the torus, the presence of a very strong magnetic field at small radii, and low- $l$  material trying to accrete outside the torus. The tension of the magnetic field tries to stop the gas incoming from the torus. Once the torus accretes too slowly the magnetic tension causes to the field lines to straighten and seals off the black hole because a highly magnetized cylinder forms around it. At this stage, gas flowing through the torus is constrained to move roughly parallel to the polar axis. This continues until enough low- $l$  gas builds up in the torus to overcome the tension of the magnetic cylinder.

Despite the differences in the flow in these various states, there are many properties of the flow that stay unchanged. We allow the entropy of gas to increase due to nonadiabatic heating caused by the artificial viscosity in run D. However, we note that the entropy is increased only inside the polar flow and is nearly constant inside the torus. This property indicates that MRI, not convection, is responsible for the complex nature of the flow. In particular, the vigorous circulation inside the torus is driven by MRI. The same is true when resistive heating is switched on (e.g., run F). In the discussion of the flow at large radii (Figure 1), we noted that despite complex velocity and magnetic fields the flow rotates on cylinders. Figs. 4–7 show that this property holds even at small radii, as indicated by the contours of  $\Omega$  parallel to the rotation axis. The contours of specific angular momentum reveal that most of the changes in  $l$  occur near the equator just outside the torus. Specifically,  $l$  decreases from 1 to 0 with decreasing radius near the equator. However, inside the torus,  $l$  remains nearly constant with clear indication of some regions with  $l > 1$ ! The very fact that we observe regions inside the torus with  $l > 1$  indicates the outward transport of  $l$  because our initial and boundary conditions do not introduce any material with  $l > 1$ . In passing, we note that we decided to consider a step function for the angular distribution of  $l$  because we wish to see as clearly as possible the evolution of  $l$ .

We start our simulation with a very weak magnetic field and very slow rotation. Although our flow rotates differentially, the initial rotation is far from Keplerian in its values as well as its dependence on radius. The latter scales like  $r^{-2}$ , typical for a constant angular momentum fluid, rather than like  $r^{-1.5}$  as for a Keplerian disk. In fact, our initial conditions are such that Keplerian rotation is reached only at  $2R_S$ . Since MRI is driven by the free energy in differential rotation, we have analyzed our solution in great detail to check whether MRI is indeed responsible for the nature of our flow. In particular, we have checked that the flow (the torus, more precisely) is subject to MRI for the actual rotational profile and the strength of the magnetic field (see eq. 108 in Balbus & Hawley 1998) and that our numerical resolution is adequate to follow the growth and saturation of MRI. Our analysis shows that most of the inner torus is unstable and that we are able to resolve, although marginally, the fastest growing MRI mode inside the inner torus. The wavelength of the mode is  $\lambda_c = 2\pi v_A / \sqrt{3}\Omega$ . For example, in run D we find that over most of the central region of the torus  $\lambda_c / \Delta x \sim 4$  but there are also regions with  $\lambda_c / \Delta x \sim 100$  and with  $\lambda_c / \Delta x \lesssim 1$ .

To investigate the nature of our solutions in more detail, we have performed some simulations with a higher resolution near the equator, where MRI is expected to be most important. We find that our test run E, with  $d\theta_l/d\theta_{l+1} = 1.02$  for  $0^\circ \leq \theta \leq 90^\circ$  (i.e., the zone spacing is decreasing toward the equator in this region) and  $d\theta_{l+1}/d\theta_l = 1.02$  for  $90^\circ \leq \theta \leq 180^\circ$ , gives very similar results to those from run D. Additional confirmation of our interpretation of the results can be found by comparing them with expected

scaling relations and with other relevant published results. Therefore, we will now present our results in a form similar to that presented by SP01. As will be clear from the following figures, our results resemble the other results despite significantly different initial and outer boundary conditions. Generally, we find that once MRI starts to operate it totally determines the nature of the flow.

Figure 9 shows the radial profiles of several quantities in run D, angle-averaged over a small wedge near the equator (between  $\theta = 87^\circ$  and  $93^\circ$ ), and time-averaged over 12 data files covering a period when accretion is nearly steady and occurs only through the torus (i.e., orbits 2.388 through 2.417; see Fig. 3a). We can compare this plot directly with Figure 6 in SP01 for their run F. We indicate the location of the last stable circular orbit by the vertical dotted line in each panel.

As in the MHD models of SP01, the profiles of each variable are not simple power-laws but are rather complex. In particular, for  $r' \lesssim 0.01$  the density is nearly constant whereas for larger radii it decreases with increasing radius almost as  $r^{-1}$ . However, we note that this power-law at large radii is a relict of the initial conditions, i.e., the subsonic part of the Bondi inflow with a PW potential. The gas pressure is higher than the magnetic pressure for large radii. However, for  $r' \lesssim 0.004$  the two pressures are comparable. For  $r' > 0.004$ , the magnetic pressure decreases with increasing radius much faster than the gas pressure. The rotational velocity is always sub-Keplerian. However, it peaks at nearly the Keplerian value for  $r' = 0.006$ . For  $r' > 0.006$ , the rotational velocity scales as  $r'^{-2}$  as for the angular momentum conserving fluid.

To measure the Reynolds stress, we follow Hawley (2000, see also SP01) and compute the difference between the angular momentum flux and mass flux times the mean angular momentum:

$$\langle \rho v_r \delta v_\phi \rangle = \langle \rho v_r v_\phi \rangle - \langle \rho v_r \rangle \langle v_\phi \rangle, \quad (14)$$

and then normalize it to the gas pressure:

$$\alpha_{gas} = \langle \rho v_r \delta v_\phi \rangle / \langle P \rangle. \quad (15)$$

We find that for  $r' < 0.002$  the normalized Reynolds stress is negative and decreases sharply with decreasing radius (note that Figure 9 shows only the magnitude of the normalized Reynolds stress). For  $r' > 0.002$ , the normalized Reynolds stress is positive, peaks at 0.15 for  $r' \sim 0.0025$  and decreases with increases radius, for  $r' \lesssim 0.0045$ . Beyond  $r' \sim 0.0045$ ,  $\alpha_{gas}$  stays positive but is very small. On the other hand, the Maxwell stress, normalized to the magnetic pressure,  $\alpha_{mag} \equiv \langle 2B_r B_\phi \rangle / \langle B^2 \rangle$ , is negative for all radii except for a small radial range around  $r' = 0.027$  (note a local minimum in Fig. 9). Comparing the actual stresses rather than the ‘alphas’ (i.e.,  $\langle \rho v_r \delta v_\phi \rangle$  vs.  $\langle B_r B_\phi / 2 \rangle$ ), we find that the Maxwell stress transports angular momentum outward and is stronger than the Reynolds stress.

The last panel in Figure 9 shows that the toroidal component of the magnetic field is dominant at all radii. However, for  $r' \lesssim 0.004$ , the radial component increases with decreasing radius and becomes comparable with the toroidal field.

Overall, we find that the properties of the inner flow of our run D are strikingly similar to those found by SP01 in their run F. The main differences occur for very small radii ( $r' < 0.004$ ). For example, we find weaker advection of such quantities as angular momentum by the infalling gas. This is consistent with the fact that in SP01 simulations, the torus accretes almost steadily (at least at small radii) whereas we find a very strong poloidal magnetic field parallel to the rotation axis, which tends to interrupt the torus accretion at small radii.

### 3.2. Dependence of accretion flow properties on $\beta_o$

Our simulations with an initial magnetic field weaker than that for run D (i.e.,  $\beta_o > 10^6$ ) show that the accretion flow is qualitatively insensitive to  $\beta_o$ . The main difference is in the time it takes the torus corona and outflow to push away the low- $l$  material inflowing in the polar funnel. In particular, our simulations for  $\beta_o = 10^7$  (run G) show that the polar funnel accretion is stopped only after  $\sim 1$  orbit (see Fig. 2). Before that time, the accretion flow is similar to its inviscid HD counterpart: accretion occurs through a polar funnel where  $l < 1$ . The shape of the funnel and  $\dot{M}_a$  are determined by the shape of a torus where there is little accretion ( $\dot{M}_a = 0.2$  but the torus contribution is less than 1%). Only when the torus corona and outflow become well-developed do they shut off accretion through the funnel. Other differences between run G and D are: (i) at the end of run G, the torus accretion rate is lower than for run D and (ii) in run G, the torus accretion is not interrupted by the magnetic field at small radii. The decrease of  $\dot{M}_a$  via the torus with increasing  $\beta$  has been found before (e.g., SP01). We attribute the disappearance of dips in  $\dot{M}_a$  to the fact that the polar funnel is more sensitive than the torus to the initial and outer boundary magnetic field. In particular, the magnetic field in the torus is amplified both by MRI and by shear and is less dependent on the initial and outer conditions than the magnetic field in the polar funnel, which is amplified by accretion of the initial field.

For  $\beta_o < 10^6$ , the initial magnetic field is too strong to be consistent with our initial requirement of weak magnetic fields (e.g., run C). The main inconsistency is due to the fact that for  $\beta_o < 10^6$  the torsional waves are faster than the flow. Consequently, the waves reach the inner boundary before the material with  $l > 0$  and the inner flow is disrupted by the waves reflected from the inner boundary. We observe a train of persistent shocks propagating outward which prevent the non-zero  $l$  material from reaching small radii.

We conclude that the accretion flow in run D, which we described in detail in the previous section, is a representative solution for a range of magnetic fields in the weak field regime, and is not just applicable to one particular initial field strength. Next we discuss our results for various  $l_0$  and demonstrate that the generic features of run D appear to be robust and apply to a wide range of conditions.

### 3.3. Dependence of accretion flow properties on $l_0$

Our choice of  $l_0 = 1$  and a step function for the angular distribution of  $l$  in run D was motivated by a wish to see if even a minimal angular momentum can reduce the mass accretion rate. We note that by setting  $l_0 = 1$  we created rather unfavorable conditions for MRI to grow because the rotational velocity is sub-Keplerian in the whole computational domain except at  $r = 2R_S$ . As we showed above, MRI is very robust and dominates the nature of the flow even for sub-Keplerian rotation.

In reality the angular momentum distribution beyond the Bondi radius is likely to be complex. In particular, we expect a large range of  $l$ . Numerical experiments, such as ours, try to isolate the key elements of the accretion flow. For example, Stone et al. (1999), SP01, Hawley, Balbus & Stone (2001), and Hawley & Balbus (2002) considered a constant angular momentum hydrostatic torus for their initial conditions. Contrary to us, they assumed a larger angular momentum so that the circularization radius is larger than the black hole radius by a factor of few or more.

To make more direct contact with those previous simulations, we ran a couple of simulations with  $l = 4R_{Sc}$  (runs I and J). We expect that a higher  $l$  will result in the development of a Keplerian flow for large radii, as the circularization radius is  $8R_S$  and MRI will be needed to transfer angular momentum.

Our run J is an HD inviscid accretion flow and serves as a reference run. We find that run J is

consistent with our other inviscid HD accretion runs performed for PB03. Namely, we observe the formation of a torus with  $l > 2R_{Sc}$ , via which there is no accretion but the shape of which determines the geometry and  $\dot{M}_a$  of a polar accretion funnel. The funnel accretion and its  $\dot{M}_a$  settle into a steady state after  $t \sim 0.6$ . The torus exhibits subsonic circulation. The specific angular momentum in the funnel is practically zero, as expected. The torus rotates on cylinders and  $l$  increases from  $2R_{Sc}$  to  $4R_{Sc}$  with increasing radius for  $r' \lesssim 0.1$  at the end of our simulations. Beyond 0.1,  $l$  is constant. The gradual change of  $l$  inside the torus is caused by a mixing of the zero  $l$  and non-zero  $l$  material during the initial phase of the evolution. During the later phase, the material with  $2R_{Sc} \leq l \leq 4R_{Sc}$  remains in the torus as it cannot be accreted.

Run I is similar to run J with the exception that we added a magnetic field ( $\beta_o = 10^6$ ). In the early stages of run I, the flow consists of an accretion funnel and a torus. As in run J,  $l = 0$  in the funnel and the torus is made of the material with  $l > 2R_{Sc}$ . However, contrary to its inviscid counterpart, the torus in run I accretes onto the black hole due to MRI. Qualitatively, run I is similar to runs D and G. The main difference is in the duration of the phase when both the torus and polar funnel accrete (i.e., for run I it lasts for  $\sim 2$  orbits while for run D the duration is  $\sim 0.3$  and for run G it is  $\sim 1.3$ ).

Figure 10 presents the radial profiles of several quantities in run I angle-averaged over a small wedge near the equator (between  $\theta = 87^\circ$  and  $93^\circ$ ), and time-averaged over 20 data files covering a period when accretion is nearly steady and occurs only through the torus (i.e., orbits 2.35 through 2.40). We can compare this plot directly with our Figure 9 and with Figure 6 in SP01 for their run F. As expected, run I is even more similar to SP01's run F than it is to run D. In particular, we find that in run I the rotational velocity is close to Keplerian for quite a wide range of radii. This is a clear indication of the outward transport of angular momentum. We note that for small radii ( $0.003 \lesssim r' \lesssim 0.02$ ), the density profile in run I scales almost as  $r'^{-1/2}$  and the density is lower than in run D for the same radii. However, we would be very cautious about drawing any conclusions from this scaling because of the relatively small range of radii in our computational domain (see Section 4).

Finally, we comment on our runs B and A with zero- $l$  material which are simply magnetized Bondi flows. We consider these runs as tests of our code. Because these runs are for weak magnetic fields ( $\beta = 10^6$  and  $10^5$  for run B and A, respectively), they should be very similar to the Bondi flow (see PB03). Our simulations show that the mass accretion rate is indeed equal to the Bondi rate and the flow is almost spherically symmetric. The departure from spherical symmetry is due to numerical resistivity (in both runs) and artificial resistivity in run A. However, the heating caused by magnetic field reconnection is limited to the region very close to the equator and is very low, i.e., the maximum increase of entropy is on the equator at the inner radius,  $r_i$ , and is 0.3 per cent for run B, and 2 per cent for run A.

#### 4. Discussion

This paper presents the second phase of our study of slightly rotating accretion flows onto black holes where, in contrast to our previous paper, we have included magnetic fields. By adding MHD effects, we can calculate turbulent stresses generated self-consistently by MRI and thus include the transport of energy and angular momentum outward as needed to accrete matter with a specific angular momentum higher than  $2R_{Sc}$ . Our simulations support strongly our hypothesis that even very slow rotation of gas at large radii may be sufficient to reduce the mass accretion rate to the level required by observations. In what follows we will summarize our results, briefly review the limitations of our work, and discuss how the physical effects neglected here may change the results.

We have performed numerical 2D, axisymmetric, MHD simulations of rotating accretion flows onto a black hole. Our simulations are complementary to previous MHD simulations which considered strongly rotating accretion flows. We consider slightly rotating flows and attempt to mimic the boundary conditions of classic Bondi accretion flows as modified by the introduction of a small, latitude-dependent angular momentum at the outer boundary, a pseudo-Newtonian gravitational potential and weak poloidal magnetic fields. A weak radial magnetic field and the distribution of  $l$  with latitude allow the density distribution at infinity to approach spherical symmetry. The main result of our simulations is that the nature of the accretion flow is totally controlled by magnetic fields when  $l \gtrsim 2R_{Sc}$ . As in the HD inviscid case, which we studied in PB03, the material with  $l \gtrsim 2R_{Sc}$  forms an equatorial torus. However, in the MHD case, the torus accretes onto the black hole because of MRI and produces both a corona and an outflow. We find that the latter two can be strong enough to prevent accretion of the low- $l$  material through the polar regions, the source of accretion in the HD inviscid case. The net mass accretion rate through the torus is lower than the Bondi rate and also lower than the accretion rate in the HD inviscid case. In PB03, we found that in order to reduce the mass accretion rate in the HD inviscid case, the polar accretion funnel had to be much narrower than the funnels allowed by a hydrostatic  $l = 2R_{Sc}$  torus. Here we find that the outflow and corona produced by the accreting torus are natural mechanisms to narrow or even totally close the polar funnel for the accretion of the low- $l$  material. We conclude that the inclusion of even slow rotational motion of the MHD flow at large radii can significantly reduce  $\dot{M}_a$  compared to the Bondi rate.

The accreting torus is the crucial component of our accretion flow, therefore we describe its main properties in more detail. Overall, the inner flow consists of a turbulent, gas pressure-dominated MHD torus with an outflow or corona or both, bounded by a magnetic pressure-dominated polar flow. The torus accretes near the equator. The accretion through the torus can be supplemented, in a quasi-periodic manner, by the low- $l$  material in the polar regions. In fact,  $\dot{M}_a$  due to this polar accretion can be one order of magnitude larger than that due to the torus. The ‘off torus’ accretion is a manifestation of the facts that our initial and outer boundary conditions allow the zero- $l$  material to approach the black hole and that the torus corona and outflow are not always strong enough to push it away. Accretion through the torus can also be interrupted for a short time by strong poloidal magnetic field that builds up during accretion. However, we observe that even during periods when the torus is truncated, there is inflow of material inside the torus and its mass and pressure build up. Consequently, the magnetic field is quickly pushed inward by the torus and the gas from the torus can again fall onto the black hole. Thus, our simulations show a strong buildup of the poloidal magnetic field as in Igumenshchev, Narayan & Abramowicz (2003) but here we find that it is a transient and not a final solution.

Hawley & Balbus (2002) identified three well-defined dynamical components in their simulations of 3D MHD accretion flows: (i) a hot, thick, rotationally dominated Keplerian disk, (ii) a surrounding magnetized corona with vigorous circulation and outflow, and (iii) a magnetically confined jet along the centrifugal funnel. We also observe these three components in cases where the circularization radius is well outside the black hole, i.e., in cases similar to those studied by Hawley & Balbus (2002; see also SP01). We conclude that the three-component accretion flow is robust at small radii, despite the fact that we also allow for low- $l$  material at large radii.

We note that  $R'_S$  in our simulations is much larger than that in real systems, where it is  $10^{-5}$  and smaller. Additionally, our relatively large  $R'_S$  and high  $\gamma$  do not allow us to capture, over a great radial range, the asymptotic behavior of the Bondi accretion flow, i.e., the flow in free fall yielding a steep ( $\propto r^{-3/2}$ ) density profile. The free fall approximation is valid for radii small compared to the sonic point,  $x_s$ . However, our choice of  $R'_S$  and  $\gamma$  yield  $x_s = 0.027$  (PB03). Thus the approximation that  $\rho \propto r^{-3/2}$

is valid over less than one order of magnitude in radius. This radial range is additionally reduced at very small radii because the free fall velocity in the PW potential is higher than for the Newtonian potential, so that the density profile is flatter than  $\rho \propto r^{-3/2}$  for very small radii. For slightly rotating flows as in real systems, we lack analytic predictions. Therefore, we treat our simulations only as first-order indications of what may be happening in real systems. In particular, we find that our accretion flows differ significantly from advection-dominated accretion flows (ADAF) solutions. For example, ADAF solutions predict nearly spherically symmetric inflows with a steep density profile, whereas we find a thick torus with a flat ( $\sim r^{-1/2}$ ) density profile. Our solutions differ also from convection-dominated accretion flows (CDAF) solutions as we find an MHD turbulent torus with an outflow instead of a convection-driven closed circulation. Our solutions appear to be MHD analogs of the HD viscid self-similar solutions of Blandford & Begelman (1999), where inflows as well as outflows of gas play a critical role in determining the properties of the accretion flow.

Our simulations do not include some of the physical processes that may be important in accretion flows onto black holes. Additionally, we have performed our simulations in 2D instead of 3D. Thus, in our simulations, a poloidal magnetic field can eventually dissipate according to the antidynamo theorem (e.g., Moffatt 1978). Additionally, we can not simulate the toroidal field MRI and we may be emphasizing the “channel” solution mode (Hawley & Balbus 1992) which produces coherent streaming in the disk plane instead of more generic MHD turbulence. Obviously, 3D MHD simulations are required. However, one should not underestimate the importance of the larger radial dynamic range and time scale afforded by 2D simulations if one wants to make direct contact with observations and with theoretical models which often yield self-similar solutions. Future work should also include studies of accretion flows with various initial configurations of the magnetic field.

ACKNOWLEDGMENTS: We thank J.M. Stone for useful discussions. DP acknowledges support from NASA under LTSA grant NAG5-11736 and support provided by NASA through grant AR-09532 from the Space Telescope Science Institute, which is operated by the Association of Universities for Research in Astronomy, Inc., under NASA contract NAS5-26555. MB acknowledges support from NSF grant AST-9876887.

## REFERENCES

- Abramowicz, M.A., Chen, X., Kato, S., Lasota, J.-P., Regev, O. 1995, *ApJ*, 438, L37
- Abramowicz, M.A., Igumenshchev, I. V., Quataert, E., & Narayan, R. 2002, *ApJ*, 565, 1101
- Balbus, S.A., & Hawley, J.F. 1998, *Rev. Mod. Phys.*, 70, 1.
- Balbus, S.A., & Hawley, J.F. 2002, *ApJ*, 573, 749
- Begelman, M.C., & Meier, D.L. 1982, *ApJ*, 253, 873
- Blandford, R.D., & Begelman, M.C. 1999, *MNRAS*, 303, L1
- Blandford, R.D., & Begelman, M.C. 2002a, in preparation
- Blandford, R.D., & Begelman, M.C. 2002b, in preparation
- Bondi, H. 1952, *MNRAS*, 112, 195
- Di Matteo, T., Allen, S.W., Fabian, A.C., Wilson, A.S., & Young, A.J. 2003, *ApJ*, 582, 133
- Di Matteo, T., Carilli, C.L., & Fabian, A.C. 2001, *ApJ*, 547, 731
- Di Matteo, T., Fabian, A.C., Rees, M.J., Carilli, C. L., & Ivison, R.J. 1999, *MNRAS*, 305, 492
- Di Matteo, T., Quataert, E., Allen, S.W., Narayan, R., & Fabian, A. C. 2000 *MNRAS*, 311, 507
- Fabbiano, G., Elvis, M., Markoff, S., Siemiginowska, A., Pellegrini, S., Zezas, A., Nicastro, F., Trinchieri, G., & McDowell, J., 2003, *ApJ*, in press (astro-ph/0301297)
- Hawley, J.F. 1992, *ApJ*, 528, 462
- Hawley, J.F., & Balbus, S.A. 1992, *ApJ*, 400, 595
- Hawley, J.F., & Balbus, S.A. 2002, *ApJ*, 573, 749
- Hawley, J.F., Balbus, S.A., & Stone, J.M. 2001, *ApJ*, 554, L49
- Ichimaru, S. 1977, *ApJ*, 214, 840.
- Igumenshchev, I.V., & Abramowicz, M.A. 1999, *MNRAS*, 303, 309
- Igumenshchev, I.V. & Narayan, R. 2002, *ApJ*, 566, 137
- Igumenshchev, I.V., Narayan, R., & Abramowicz M.A. 2003, *ApJ*, submitted (astro-ph/0301402)
- Loewenstein, M., Mushotzky, R.F., Angelini, L., Arnaud, K.A., & Quataert, E. 2001, *ApJ*, 555, L21
- Machida, M., Matsumoto, R., & Mineshige, S. 2001, *PASJ*, 53, L1
- Melia, F. & Falcke, H. 2001, *ARA&A*, 39, 309
- McKinney, J.C. & Gammie, C.F. 2002, *ApJ*, 573, 728
- Moffatt, K. 1978, *Magnetic Field Generation in Electrically Conducting Fluids* (Cambridge: Cambridge Univ. Press)
- Narayan, R., Igumenshchev, I.V., & Abramowicz, M.A. 2000, *ApJ*, 539, 798



- Narayan, R., Quataert E., Igumenshchev, I.V., & Abramowicz, M.A. 2002, ApJ, 577, 295
- Narayan, R., & Yi, I. 1994, ApJ, 428, L13
- Narayan, R., & Yi, I. 1995, ApJ, 444, 231
- Ostriker, J.P., McCray, R., Weaver, R., & Yahil, A. 1976, ApJ, 208, L61
- Paczyński, B., & Wiita, J.P. 1980, A&A, 88, 23
- Proga, D., & Begelman M.C. 2003, ApJ, 582, 69 (PB03)
- Quataert, E., & Gruzinov A. 2000, ApJ, 545, 842
- Quataert, E., & Narayan R. 1999, ApJ, 520, 298
- Rees, M.J., Begelman, M.C., Blandford, R.D., & Phinney, E.S. 1982, Nature, 295, 17
- Stone, J.M., & Norman, M.L. 1992a, ApJS, 80, 753
- Stone, J.M., & Norman, M.L. 1992b, ApJS, 80, 791
- Stone, J.M., & Pringle, J.E. 2001, MNRAS, 322, 461 (SP01)
- Stone, J.M., Pringle, J.E., & Begelman, M.C. 1999, MNRAS, 310, 1002

Fig. 1. A sequence of logarithmic density and angular velocity contours (left and middle panels, respectively) and velocity direction plots (right panel) from run D at times 0.11, 0.34, 0.52, 1.45, and 2.54. The minimum and maximum of  $\log \rho$  are 0.25 and 2. We use eight equally spaced contour levels for  $\log \rho$ . The angular velocity is in units of  $2c/R_S$ . The minimum of  $\log \Omega$  is -6 and seven contour levels are equally spaced at intervals of  $\Delta \log \Omega = 0.25$ . We show the direction of the velocity field by unit vectors.

Fig. 2. The time evolution of the mass accretion rate in units of the Bondi rate, for run D (solid line) and run G (dashed line). Vertical arrows mark times for run D corresponding to the snapshots shown in Figures 4, 5, 6, and 7 (arrow a, b, c, and d respectively) and in Figure 8.

Fig. 3. Late time evolution of the mass accretion rate in units of the Bondi rate, for run D (top panel) and run G (bottom panel). This figure is very similar to Fig. 2 but it shows in more detail  $\dot{M}_a$  as a function of time toward the end of the simulations. Vertical arrows mark times corresponding to the snapshots shown in Figures 5, 6, and 7 (arrow b, c, and d respectively) and in Figure 8.

Fig. 4. Two-dimensional structure of various quantities from the fiducial model (run D) near the beginning of simulations at  $t = 0.22$ , marked by arrow a in Fig. 2. At this time accretion onto the black hole occurs through both the torus and the polar funnel. The top panels from left to right are snapshots of  $\log \rho$ ,  $S$ ,  $\log \Omega$ ,  $l$ , and direction of the fluid velocity. The bottom panels from left to right are snapshots of  $\log (P + B^2/8\pi)$ ,  $\log B^2/8\pi$ ,  $\log \beta$ ,  $\log |B_\phi|$ , and direction of the poloidal magnetic field. All contour levels are equally spaced. There are eight contours for the density,  $\log \rho$ , between 0.25 and 2; nine for the entropy,  $S$ , between 40 and 44; four for the angular velocity,  $\log \Omega$ , between -2.5 and -1.75; eleven for the specific angular momentum,  $l$ , between 0.1 and 1.1 (the level for 1.1 is indicated by the dotted contour); six for the total pressure,  $\log (P + B^2/8\pi)$ , between 20.5 and 23; ten for the magnetic pressure,  $\log B^2/8\pi$ , between 17.5 and 22; seven for the plasma parameter,  $\log \beta$ , between -3 and 3 (the levels for  $\log \beta < 0$  are indicated by the dotted contours); and six for the toroidal field,  $\log |B_\phi|$ , between 7.5 and 10.

Fig. 5. Two-dimensional structure of various quantities from the fiducial model (run D) at  $t = 2.39$ , marked by arrow b in Figs. 2 and 3a. The snapshots are for the same quantities as in Fig. 4. The contour levels are also as in Fig. 4. This figure presents an example of an inner flow where accretion occurs only through the torus (see also Fig. 3a).

Fig. 6. Two-dimensional structure of various quantities from the fiducial model (run D) at  $t = 2.41$ , marked by arrow c in Figs. 2 and 3a. The snapshots are for the same quantities as in Fig. 4. The contour levels are also as in Fig. 4. This figure presents an example of an inner flow where there is no torus accretion but only very weak accretion through a very low density magnetized polar cylinder. This state is very short-lived (see Fig. 3a).

Fig. 7. Two-dimensional structure of various quantities from the fiducial model (run D) at  $t = 2.36$ , marked by arrow d in Figs. 2 and 3a. The snapshots are for the same quantities as in Fig. 4. The contour levels are also as in Fig. 4. This figure presents an example of an inner flow where accretion is dominated by low- $l$  material which managed to reach the inner boundary despite a blocking corona and outflow from the torus. The torus also accretes at this time but at a lower rate than in the low- $l$  inflow. As the low- $l$  inflow is gradually pushed away by the torus corona and outflow,  $\dot{M}_a$  slowly decreases to the level where accretion occurs only via the torus.

Fig. 8. Maps of logarithmic density overplotted by the direction of the poloidal velocity. This figure compares the inner flow in four different accretion states (see figs. 2 and 3a) shown in more detail in Figs. 4–7.

Fig. 9. Radial profiles of various quantities from run D, time-averaged from 2.388 through 2.417 orbits. During this period accretion occurs only through a torus, as illustrated in Fig. 5 (see also Fig. 3a). To construct each plot, we averaged the profiles over angle between  $\theta = 87^\circ$  and  $93^\circ$ . The top middle panel plots the gas pressure (solid line) and magnetic pressure. The top right panel plots the rotational, radial, Keplerian, and Alfvén velocities (solid, dashed, dot-dashed, and dotted line, respectively), as well as the sound speed (triple-dot dashed line). The bottom middle panel plots the Maxwell stress,  $\alpha_{mag} = 2B_r B_\phi / B^2 / P_{mag}$ , and the Reynolds stress,  $\alpha_{gas} = \langle \rho v_r \delta v_\phi \rangle / P$  (solid and dashed line, respectively). We calculate the Reynolds stress using eq. 15 and show only its amplitude. The bottom right panel plots the radial, latitudinal and toroidal components of the magnetic field (dot-dashed, dashed, and solid line, respectively).

Fig. 10. As Fig. 8 but for run I.

Table 1: Summary of parameter survey.

| Run | Resolution | $R'_S$    | $R'_C$               | $l_0$ | $\theta_o$ | $f(\theta)$   | $\beta_o$ | $Q$ | $t_f$ | $l_a^{max}$ | $\dot{M}_a/\dot{M}_B$ | Comments                         |
|-----|------------|-----------|----------------------|-------|------------|---------------|-----------|-----|-------|-------------|-----------------------|----------------------------------|
| A   | 140        | $10^{-3}$ | 0                    | 0     | 0          | —             | $10^5$    | 0.1 | 0.28  | 0.0         | 1.0                   |                                  |
| B   | 140        | $10^{-3}$ | 0                    | 0     | 0          | —             | $10^6$    | 0.1 | 0.48  | 0.0         | 1.0                   |                                  |
| C   | 140        | $10^{-3}$ | $8 \times 10^{-3}$   | 1     | $44^\circ$ | step function | $10^5$    | 0.1 | 0.1   | 0.0         | 0.05                  |                                  |
| D   | 140        | $10^{-3}$ | $8 \times 10^{-3}$   | 1     | $44^\circ$ | step function | $10^6$    | 0.0 | 2.54  | 0.0 – 0.9   | 0.025                 | fiducial run                     |
| E   | 140        | $10^{-3}$ | $8 \times 10^{-3}$   | 1     | $44^\circ$ | step function | $10^6$    | 0.0 | 0.57  | 0.0 – 0.9   | 0.058                 | $d\theta_l/d\theta_{l+1} = 1.02$ |
| F   | 140        | $10^{-3}$ | $8 \times 10^{-3}$   | 1     | $44^\circ$ | step function | $10^6$    | 0.1 | 0.32  | 0.0 – 0.9   | 0.053                 |                                  |
| G   | 140        | $10^{-3}$ | $8 \times 10^{-3}$   | 1     | $44^\circ$ | step function | $10^7$    | 0.0 | 2.51  | 0.0 – 0.9   | 0.001                 |                                  |
| H   | 140        | $10^{-3}$ | $8 \times 10^{-3}$   | 1     | $44^\circ$ | step function | $\infty$  | 0.0 | 0.64  | 0.9         | 0.17                  |                                  |
| I   | 140        | $10^{-3}$ | $3.2 \times 10^{-2}$ | 2     | $44^\circ$ | step function | $10^6$    | 0.1 | 2.54  | 0.0 – 0.9   | 0.013                 |                                  |
| J   | 140        | $10^{-3}$ | $3.2 \times 10^{-2}$ | 2     | $44^\circ$ | step function | $\infty$  | 0.1 | 0.78  | 0.0 – 0.9   | 0.27                  |                                  |

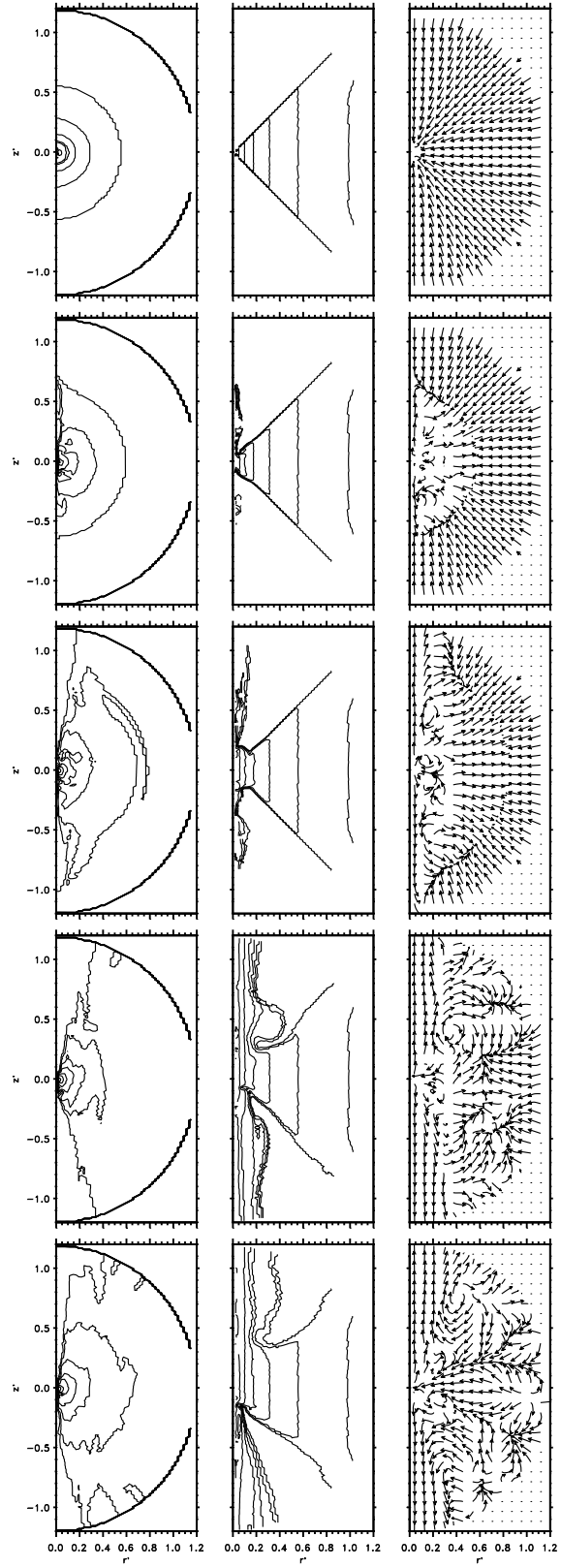


Fig. 1.—

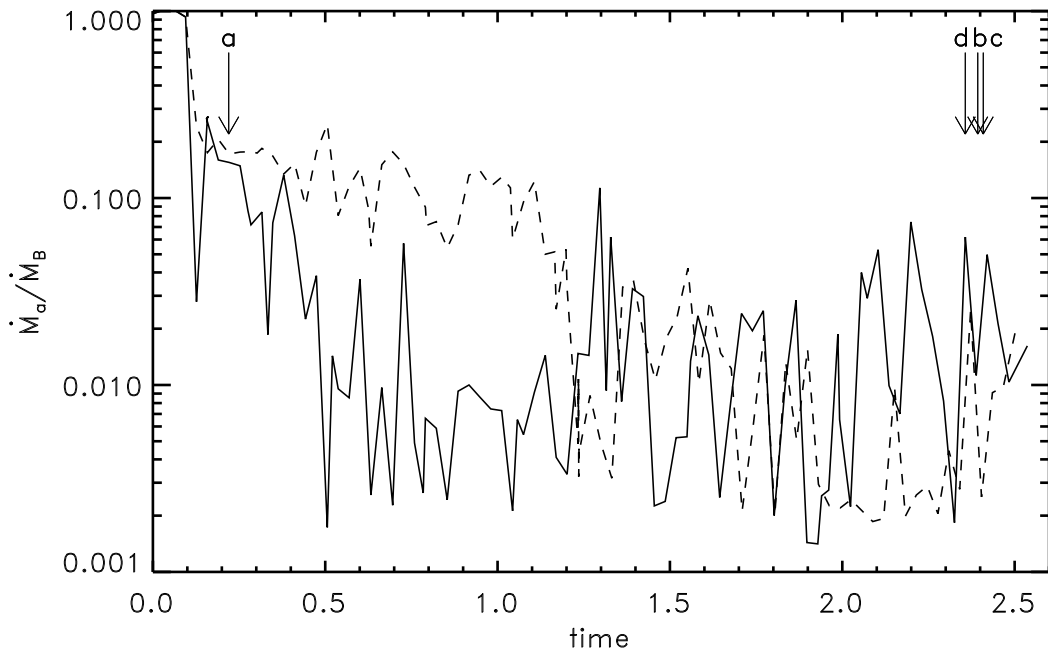


Fig. 2.—

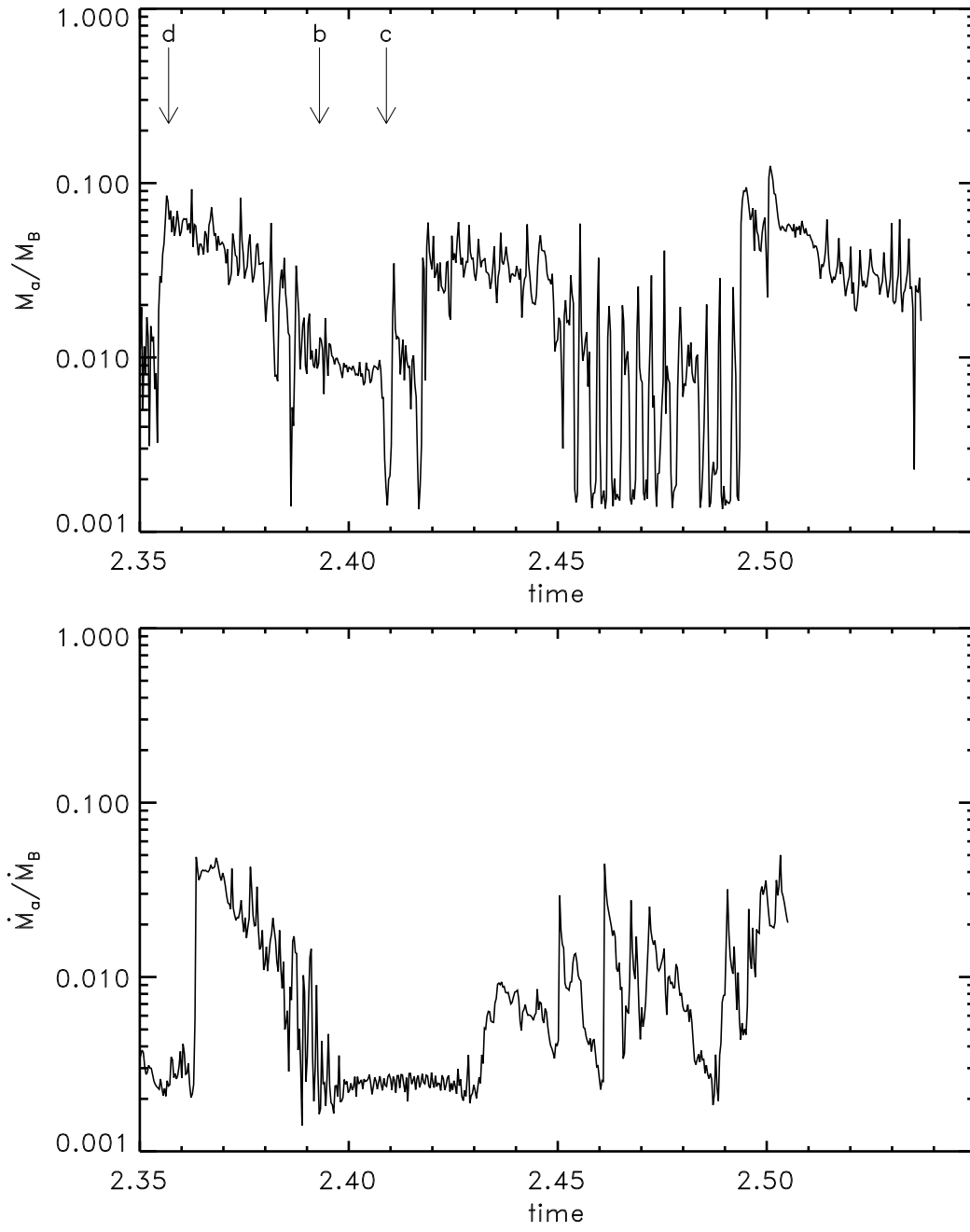


Fig. 3.—

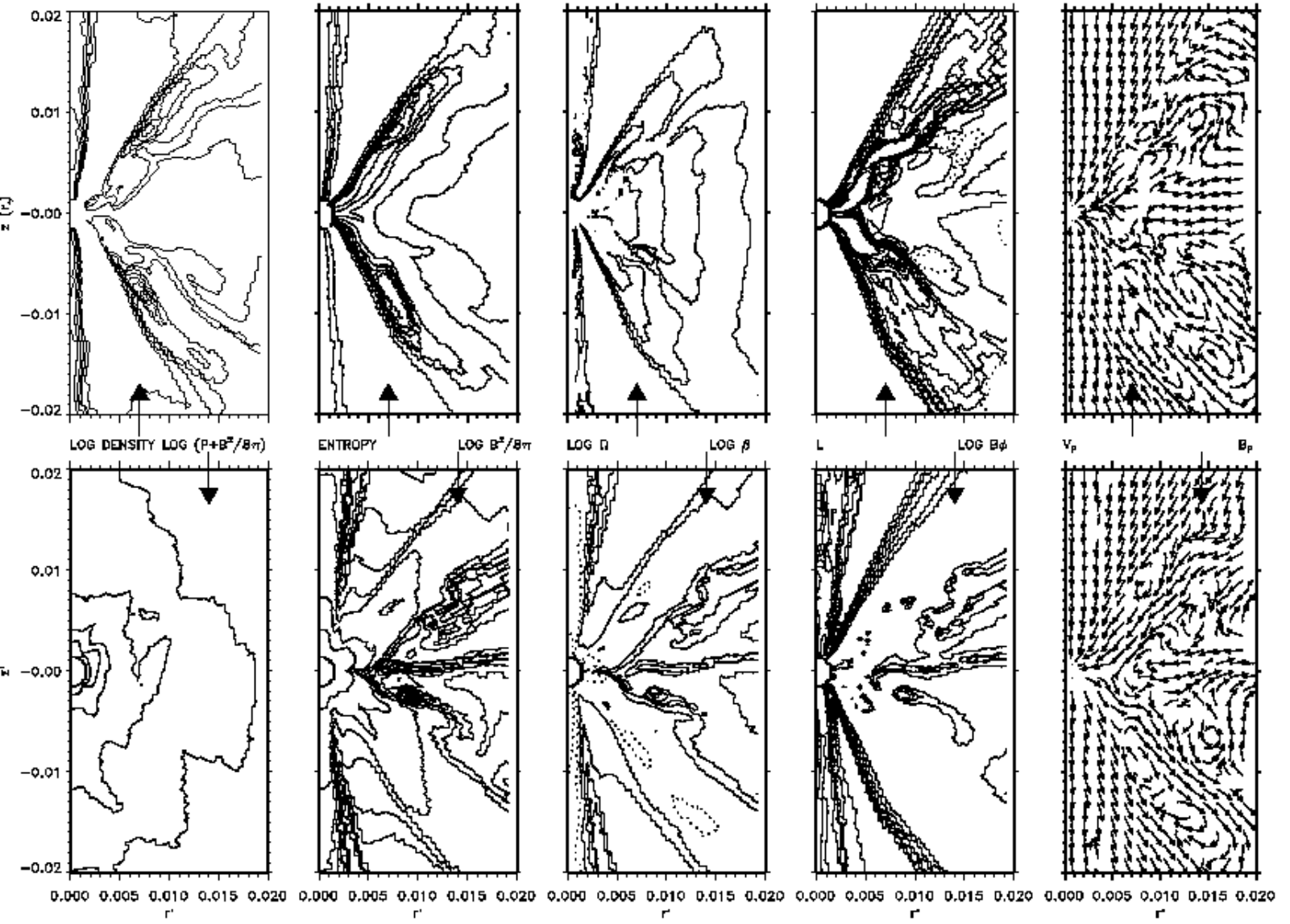


Fig. 4.—



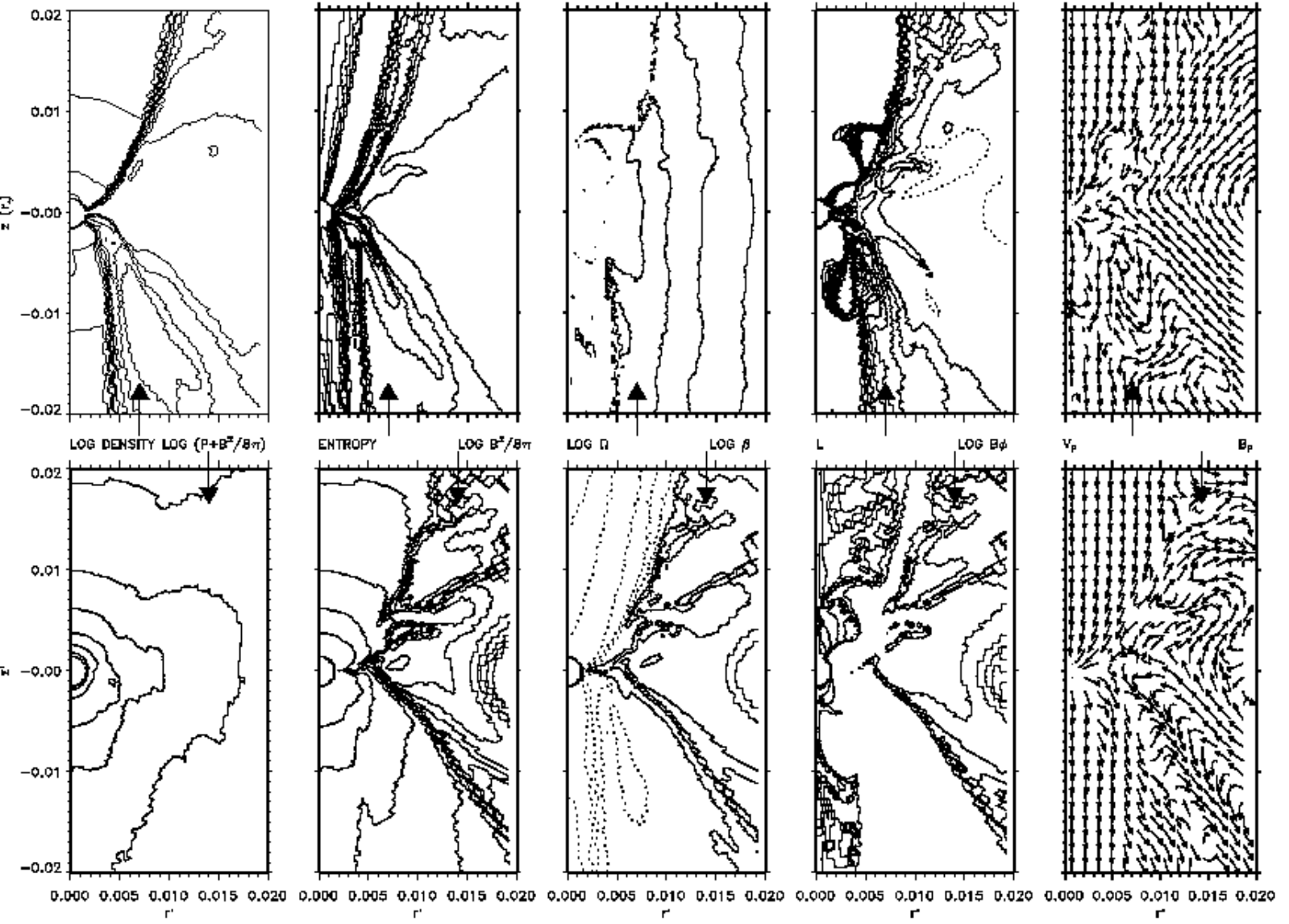


Fig. 5.—

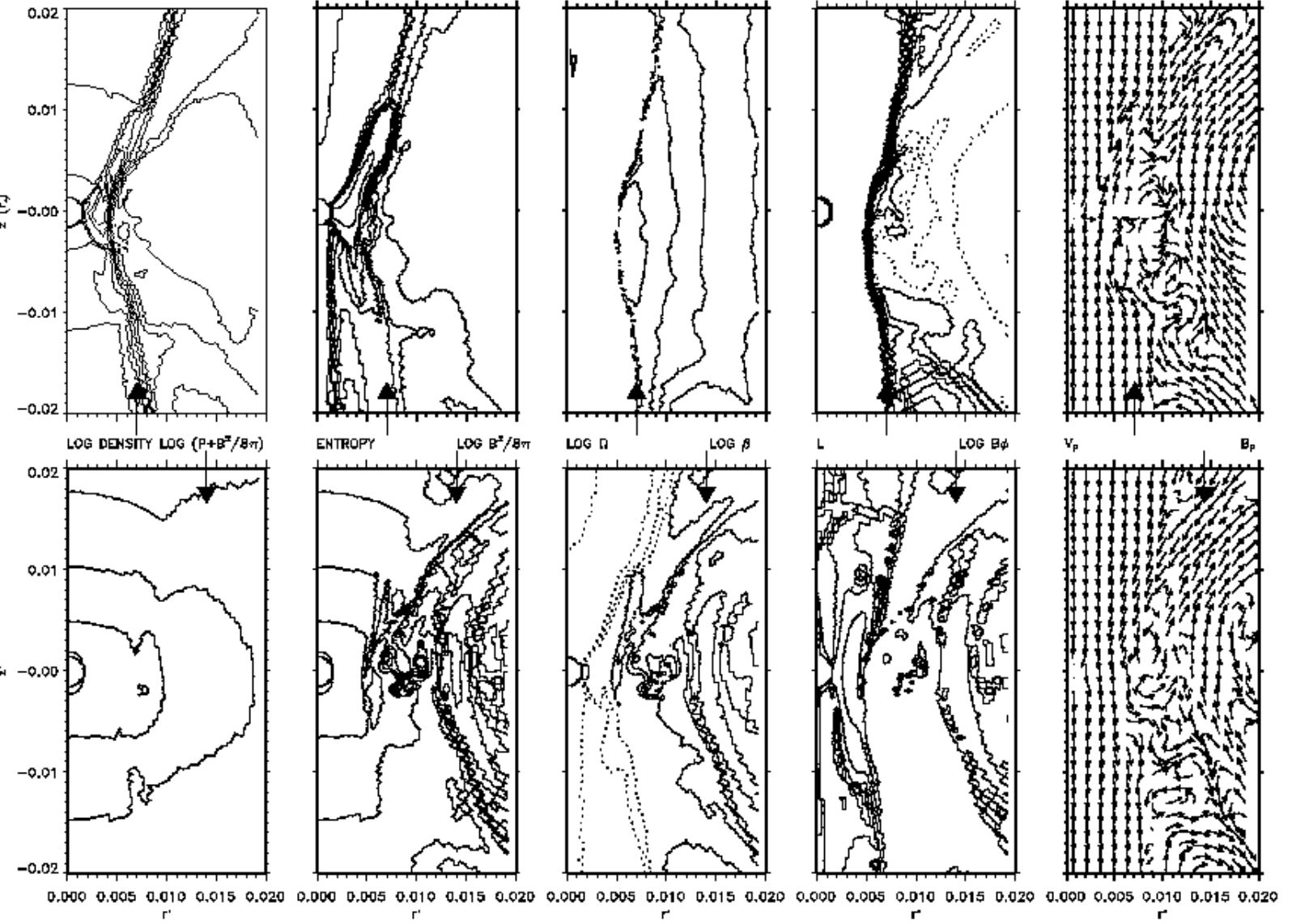


Fig. 6.—

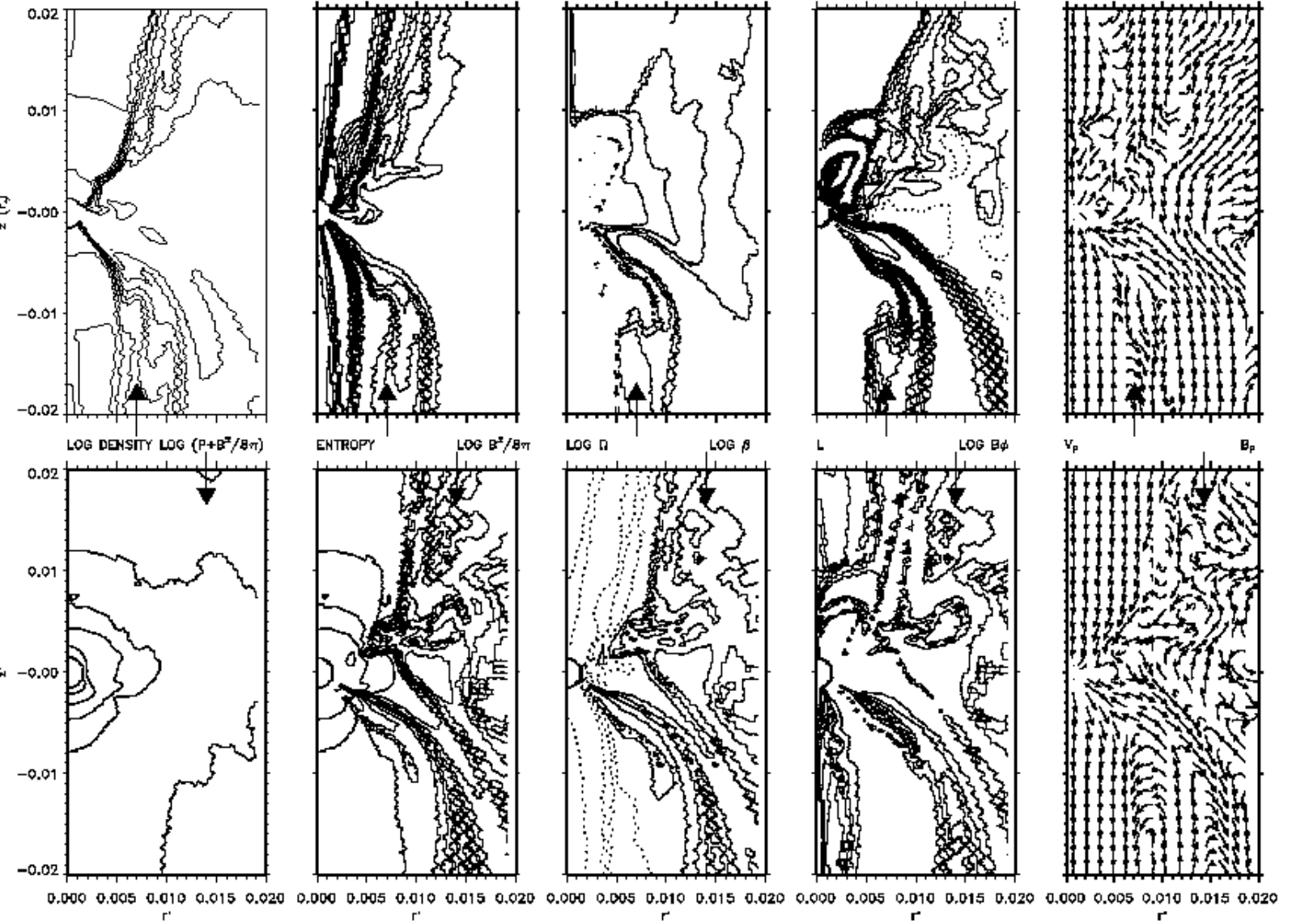


Fig. 7.—

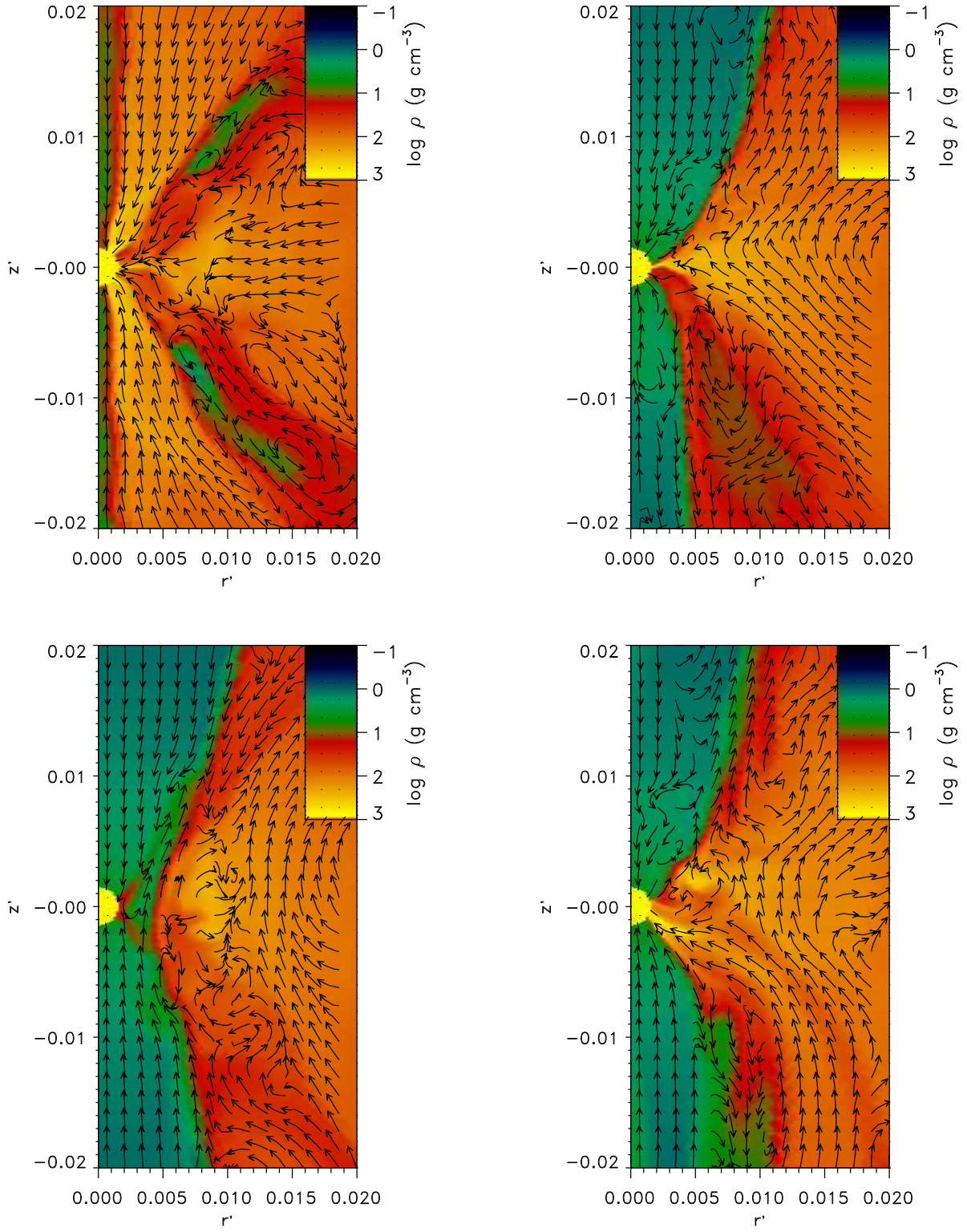


Fig. 8.—

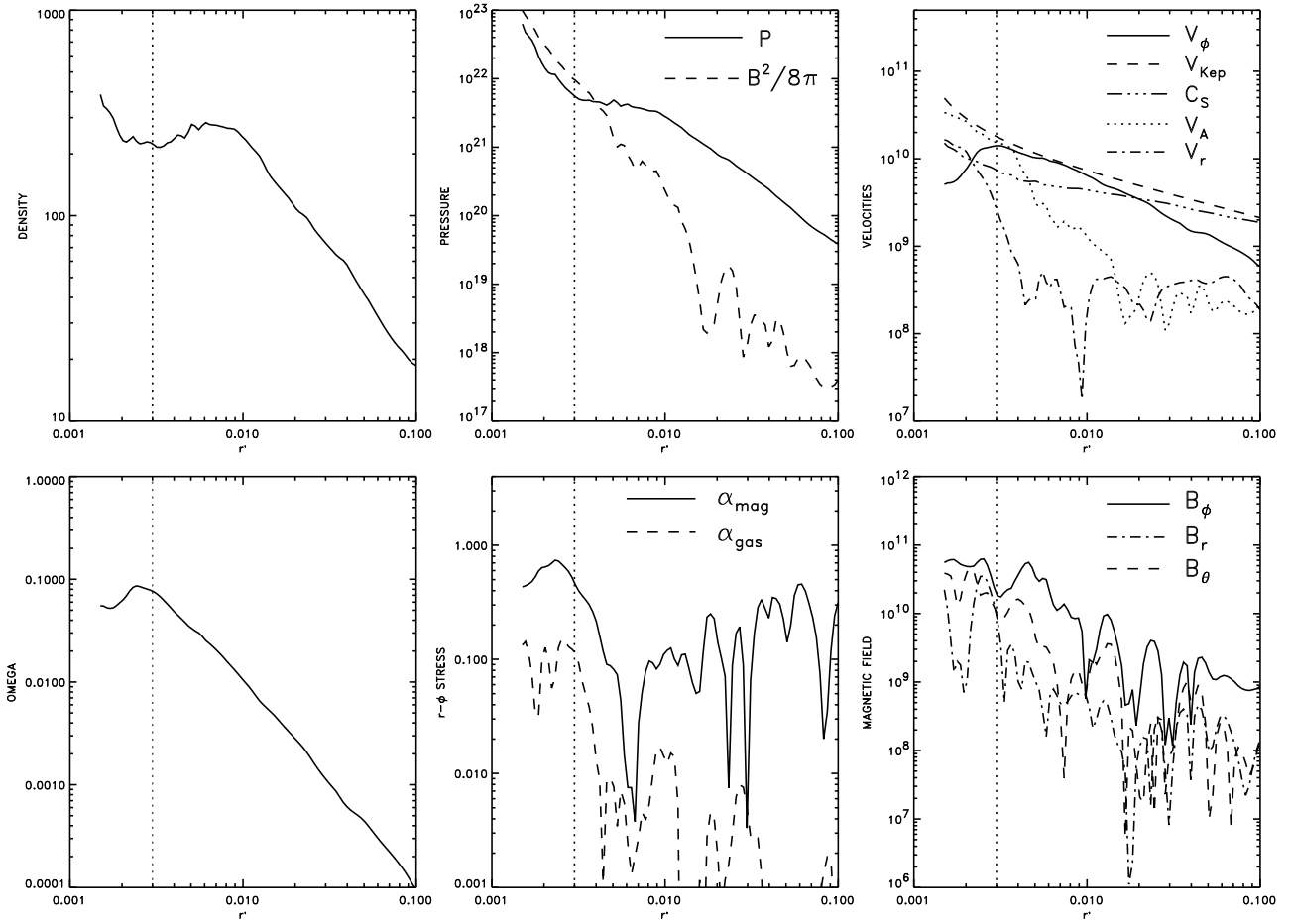


Fig. 9.—

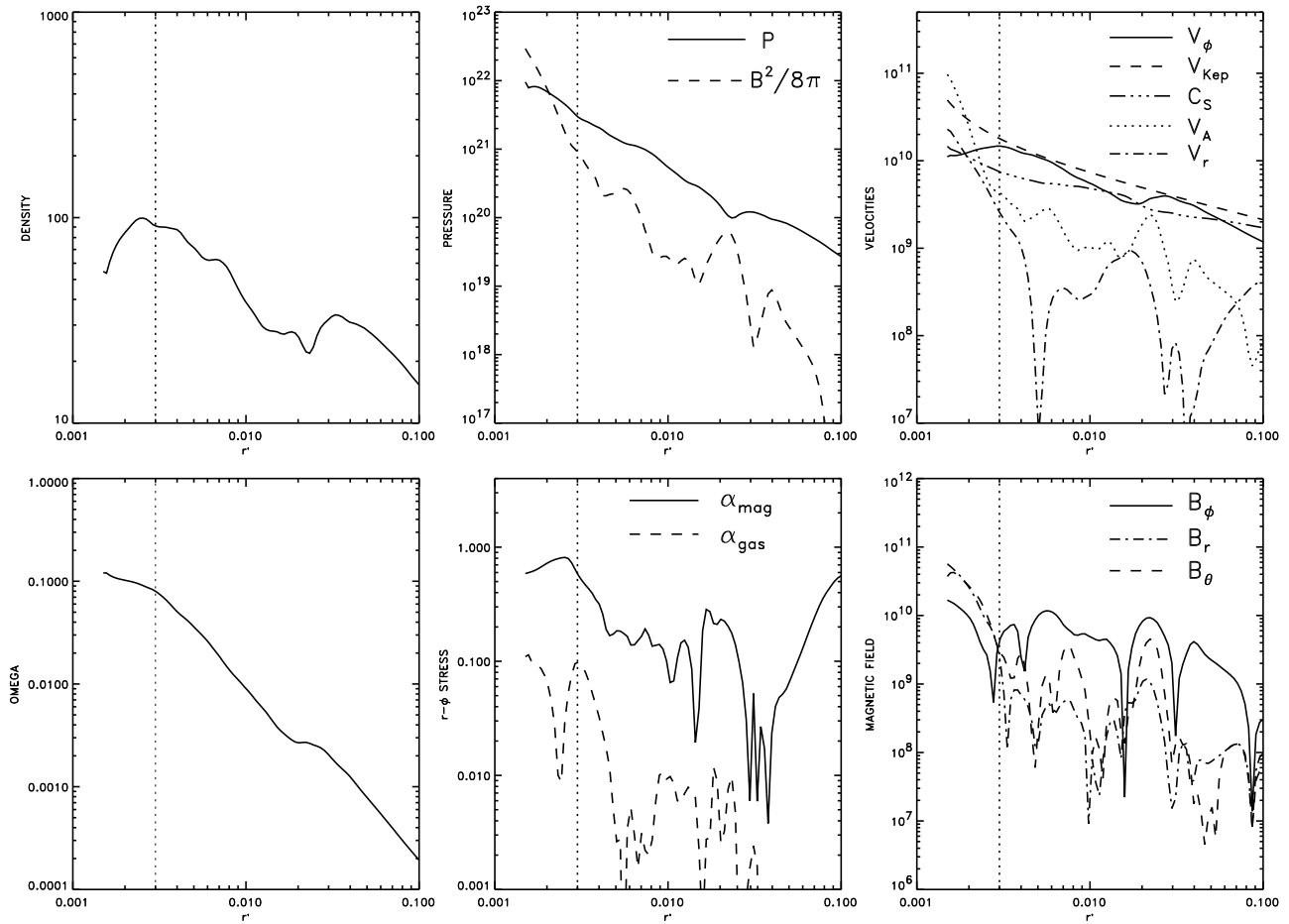


Fig. 10.—